JOURNAL OF ENVIRONMENTAL SCIENCES 135 (2024) 391–406

Available online at www.sciencedirect.com

ScienceDirect

www.elsevier.com/locate/jes

JES JOURNAL OF ENVIRONMENTAL SCIENCES

www.jesc.ac.cn

Review

Corrosion behaviors and kinetics of nanoscale zero-valent iron in water: A review

Chenliu Tang[1,**,*], *Xingyu Wang*[1,**], *Yufei Zhang*[1], *Nuo Liu*[2], *Xiang Hu*[1]

[1] *Research Group of Water Pollution Control and Water Reclamation, College of Chemical Engineering, Beijing University of Chemical Technology, Beijing 100029, China*

[2] *Shanghai Collaborative Innovation Centre for WEEE Recycling, School of Resources and Environmental Engineering, Shanghai Polytechnic University, Shanghai 201209, China*

ARTICLE INFO

Article history:
Received 8 October 2022
Revised 20 December 2022
Accepted 21 December 2022
Available online 31 December 2022

Keywords:
Nanoscale zero-valent iron (nZVI)
Corrosion behaviors
Corrosion kinetics
nZVI evolution

ABSTRACT

Knowledge on corrosion behaviors and kinetics of nanoscale zero-valent iron (nZVI) in aquatic environment is particularly significant for understanding the reactivity, longevity and stability of nZVI, as well as providing theoretical guidance for developing a cost-effective nZVI-based technology and designing large-scale applications. Herein, this review gives a holistic overview on the corrosion behaviors and kinetics of nZVI in water. Firstly, Eh-pH diagram is introduced to predict the thermodynamics trend of iron corrosion. The morphological, structural, and compositional evolution of (modified-) nZVI under different environmental conditions, assisted with microscopic and spectroscopic evidence, is then summarized. Afterwards, common analytical methods and characterization technologies are categorized to establish time-resolved corrosion kinetics of nZVI in water. Specifically, stable models for calculating the corrosion rate constant of nZVI as well as electrochemical methods for monitoring the redox reaction are discussed, emphasizing their capabilities in studying the dynamic iron corrosion processes. Finally, in the future, more efforts are encouraged to study the corrosion behaviors of nZVI in long-term practical application and further build nanoparticles with precisely tailored properties. We expect that our work can deepen the understanding of the nZVI chemistry in aquatic environment.

Introduction

In recent decades, nanotechnology has emerged as a robust option to solve environmental problems. Among the nanomaterials, core–shell structured nanoscale zero-valent iron (nZVI) serves as an excellent model nanoparticle for cost-effective contaminant transformation and separation, which is widely applied in groundwater, soil remediation and wastewater treatment (Grieger et al., 2010; Mueller et al., 2012). The nZVI extends the synergetic chemistry of nanoconstituents: a metallic iron core to provide strong reducing power for detoxification and a surface layer of iron oxides/hydroxides for contaminant attraction and sorption. A growing body of evidences have proved that nZVI can degrade and separate a variety of environmental contaminants, such as heavy metals (Huang et al., 2013; Wang et al., 2016), dyes

* Corresponding author.
E-mail: tangchenliu@buct.edu.cn (C. Tang).
** These authors contributed equally to this work.

https://doi.org/10.1016/j.jes.2022.12.028
1001-0742/

(Moon et al., 2011; Shu et al., 2007), phenolics (Kallel et al., 2009; Li et al., 2018), chlorinated compounds (Kim et al., 2010; Rajajayavel and Ghoshal, 2015), nitrate (Ryu et al., 2011; Su et al., 2014), phosphate (Wen et al., 2014), radioactive substance (Fan et al., 2013; Li et al., 2013), etc. The decontamination mechanisms include reduction (Du et al., 2016; Li et al., 2017c; Liu et al., 2017; S. Zhang et al., 2018a), oxidation (Bae et al., 2018; Gankanda et al., 2019; Hug and Leupin, 2003; Kanel et al., 2005) and adsorption/co-precipitation (Gankanda et al., 2019; Li and Zhang, 2006; O'Carroll et al., 2013; Sarathy et al., 2008; Wang et al., 2015; Yan et al., 2010a).

Concomitantly, nZVI corrosion occurs spontaneously, which poses significant impact on the reactivity, stability and long-term fate of nZVI. On the one hand, the formation of a large array of porous and highly adsorptive corrosion products (e.g., iron oxides, hydroxides, etc.) can act as reactants and remove contaminants. For example, corroded nZVI has been reported to exhibit superior adsorption ability for As(V) (Wang et al., 2017) and perfluorooctanesulfonic acid (PFOS) (Zhang et al., 2018b), even after the complete exhaustion of the pristine nZVI. On the other hand, concerns over the potential negative impact of nZVI corrosion in water have motivated numerous studies. Since nZVI is an indiscriminate reductant (Xu et al., 2021), it readily reacts and reduces water, leading to the extravagant iron corrosion. This unwanted side reaction decreases the reduction capacity of nZVI and thus shortens its reactive life-time. Tremendous efforts have thus been made to improve the iron corrosion resistance in water and prevent nZVI from unnecessary electron waste (Li et al., 2021b; Tang et al., 2020; Xu et al., 2020b). Hence, a comprehensive overview of nZVI corrosion, including the corrosion behaviors and the time-resolved corrosion kinetics, is expected to guide the rational design of nZVI with precisely tailored for specific application scenarios.

When exposed to water, the morphology, structure and chemical composition of nZVI continuously changes over time. Accordingly, the core–shell structure collapses and transforms into thin layers of sheets or bundles of needles-shaped crystals. Corrosion products are usually identified as lepidocrocite (γ-FeOOH) (Liu et al., 2017, 2014), goethite (α-FeOOH) (Kim et al., 2018; Liu et al., 2017), akaganeite (β-FeOOH) (Liu et al., 2017; Yang et al., 2019), magnetite (Fe_3O_4) (Bae et al., 2018; Wu et al., 2017b), maghemite (γ-Fe_2O_3) (Wu et al., 2017b, 2017a). Besides, evidences suggest the coexisting anions may involve in the formation of iron corrosion, such as green rusts I/II (a group of Fe(II)–Fe(III) layered double hydroxides with various interlayer anions (e.g., Cl^-, SO_4^{2-} and CO_3^{2-}) (Bae et al., 2018; Liu et al., 2014), siderite ($FeCO_3$) (Pullin et al., 2017a), vivianite ($Fe_3(PO_4)_2{\cdot}8H_2O$) (Reinsch et al., 2010; Wu et al., 2013), and iron sulfide (Fan et al., 2017; Lv et al., 2018), etc. nZVI corrosion is a complicated heterogeneous reaction, which strongly depends upon aquatic experimental conditions (e.g., dissolved oxygen, solution pH, coexisting anions and cations, natural organic matters). Moreover, emerging studies have proposed that, the modification methods and contaminants types may also influence the nZVI corrosion (Yan et al., 2010b; Li et al., 2021b; Dong et al., 2016, 2012).

Even though researchers have reviewed the progress on nZVI synthesis, modification and characterization, decontamination performance, as well as field application investigation, there is a lack of holistic overview on the corrosion behaviors and corrosion kinetics of nZVI in water when determining the final state and fate of nZVI in the environment. The main objectives of this study are to (i) summarize the morphological, structural, and compositional (modified-) nZVI evolution under different varied environmental conditions, (ii) introduce common analytical methods and characterization technologies to study the corrosion kinetics of nZVI in water, (iii) outlook the challenges and prospects of corrosion behavior monitoring in practical application. This work is expected to deepen our understanding of nZVI chemistry in aquatic environment.

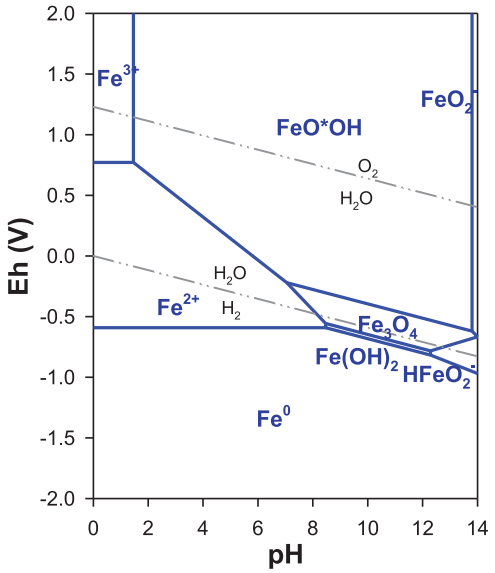

Fig. 1 – Eh-pH diagram for Fe^0/H_2O system at 298.15 K and 101.3 KPa ([Total Fe] = 10^{-4} mol/L) (Monhemius, 2017).

1. Application of Eh-pH diagram in corrosion study

Due to the physicochemical complexity of the aquatic environment, the importance of Eh-pH diagram is thus highlighted to understand the thermodynamic performance of nZVI corrosion. Eh-pH diagram, also known as Pourbaix diagram, is an electrochemical phase diagram, plotted as potential E as a function of pH (Huang, 2016; Qi et al., 2019). It indicates that, the stability of metal in solution is related to both the electrode potential and the pH of the aqueous solution (Al-Hinai et al., 2014). Hence, Eh-pH diagram has evolved as a powerful tool to reveal the thermodynamics of metal corrosion (Qi et al., 2019). The main purpose is to predict the spontaneous direction of reaction, analyze the trend of metal corrosion from thermodynamics and estimate the composition of corrosion products (Gomes et al., 2014). As shown in Fig. 1, the potential diagram of the Fe^0-H_2O system was calculated under standard conditions. From the diagram, under different equilibrium conditions, each predominance area demonstrates regions of stable species existing in a given reaction system (Li et al., 2014). It can predict the dominant species

produced under certain conditions and the possible reactions path. For example, when the potential is less than −0.6, the state of Fe^0 is stable regardless of the pH changes. However, Eh-pH diagram is a simplified ideal model, which shows regions of stable species under the standard state, but the actual situation often deviates. Environmental factors such as temperature, oxygen, and background ions can also affect the electrochemical or chemical corrosion of iron nanoparticles.

2. Corrosion behaviors of nZVI in water

As is known to all, the fresh nZVI is endowed with a sphere, typical core–shell structure. However, after contact with water, the morphology, structure and composition of nZVI has continuously changed over time, evolving to different structures (Dong et al., 2016, 2012; Liu et al., 2015). In field applications, the formation of different corrosion products will inevitably influence the reactivity, hydrodynamics and mobility of nZVI in the aquatic environment (Dong et al., 2012). Therefore, observation of the phase transformation and structural evolution of nZVI in water, which can be achieved with microscopic and spectroscopic evidence (e.g., scanning electron microscopy (SEM), transmission electron microscopy (TEM), X-ray photoelectron spectroscopy (XPS), and X-ray diffraction (XRD)), is essential to determine the reactivity and fate of nZVI in aquatic environment.

2.1. *nZVI corrosion under varied environmental conditions*

Laboratory experiments and field studies suggest that, environmental conditions (e.g., oxygen, pH, coexisting anions and cations, natural organic matter (NOM)) play a vital role in determining the corrosion behaviors of nZVI in aquatic environment (Kim et al., 2012; Liu et al., 2015; Sarathy et al., 2008; Sohn et al., 2006; Xie et al., 2014).

2.1.1. *Oxygen*

Dissolved oxygen is regarded to be of principal importance for iron corrosion. In general, under anaerobic conditions, the major corrosion products are identified as nanosheets of $Fe(OH)_2$ (Eqs. (1)–(3)) (Dong et al., 2020; Filip et al., 2014). Besides, some studies have reported the simultaneous formation of magnetite (Fe_3O_4) (Eq. (4)) (Reardon et al., 2008; Sarathy et al., 2008).

$$Fe^0 + 2H_2O \rightarrow Fe^{2+} + H_2 + 2OH^- \quad (1)$$

$$Fe^0 + H_2O \rightarrow HFeOH \quad (2)$$

$$HFeOH + H_2O \rightarrow Fe(OH)_2 + H_2 \quad (3)$$

$$6Fe(OH)_2 + O_2 \rightarrow 2Fe_3O_4 + 6H_2O \quad (4)$$

On the contrary, under anaerobic conditions, iron corrosion is substantially deteriorated, with crystalline iron (oxyhydr)oxides such as γ-FeOOH, Fe_3O_4, and γ-Fe_2O_3 as the main corrosion products (Eqs. (5)–(8)). Reinsch et al. (2010) found that a rapid (<24 hr) loss of Fe^0 when nZVI exposed to oxygen-containing water, and nZVI had corroded into both magnetite (~77%) and maghemite (~15%).

$$2Fe^0 + O_2 + 4H^+ \rightarrow 2Fe^{2+} + 2H_2O \quad (5)$$

$$4Fe^0 + 3O_2 + 2H_2O \rightarrow 4\gamma FeOOH \quad (6)$$

$$6Fe^{2+} + O_2 + 6H_2O \rightarrow 2Fe_3O_4 + 12H^+ \quad (7)$$

$$6Fe_3O_4 + O_2 + 4H^+ \rightarrow 8\gamma Fe_2O_3 + 2Fe^{2+} + 2H_2O \quad (8)$$

Beyond the presence of dissolved oxygen, reaction time and hydraulics (static and stirred) would also synergistically influence the corrosion behaviors of nZVI. As illustrated in Fig. 2, Liu's team systematically studied the evolution of nZVI in aqueous solutions with or without dissolved oxygen and under different hydraulics (static and stirred) (Liu et al., 2017, 2015, 2014). It was found that after 72 hr of aging in anoxic water, nZVI still preserved the core–shell structure, and the corrosion products were mainly wustite (FeO), goethite (α-FeOOH) and/or akaganeite (β-FeOOH). Under the static reoxygenation condition, after 10 days' aging, most of products were magnetite (Fe_3O_4) and maghemite (γ-Fe_2O_3), and lepidocrocite (γ-FeOOH). At 30 day, nZVI presented a hollow spherical structure. After 90 days, the product consisted mostly of γ-FeOOH with small amounts of Fe_3O_4 and γ-Fe_2O_3. Under the condition of stirred and reoxygenation, when aging for 24 hr, some particles were spherical with core–shell structure disappearing and the main products were Fe_3O_4, γ-Fe_2O_3 and γ-FeOOH. Under the presence of oxygen, the spheres of iron oxides evolved into flaky and/or needle-shaped phases, indicating the main product of γ-FeOOH. The corrosion of nZVI in the stirred continuous reoxygenation water was relatively rapid. After 72 hr, most of the core–shell structure of nZVI was transformed into lath-like and bundles of thin needles-shaped, and the product was mainly γ-FeOOH. It showed that under the condition of continuous stirred and sufficient oxygen, nZVI inclined to corrode into γ-FeOOH. In short, continuous stir and sufficient oxygen supply are the key factors for the collapse of "cor–shell" structure, and γ-FeOOH is the main product of long-term corrosion of nZVI in aerobic water.

2.1.2. *pH*

pH value plays a crucial role in controlling the corrosion of nZVI. Solution pH not only determines the domains of iron species in Fe-H_2O system, but also influences nZVI reactivity. In general, a low pH promotes nZVI reactivity via accelerating iron corrosion and dissolving the passivated outer layers, whereas a high pH reduces nZVI reactivity since abundant OH^- would contributes in precipitation of ferrous hydroxide on the nZVI surfaces, thus inhibiting electron transfer (Bae and Hanna, 2015; Lei et al., 2018).

Xia et al. (2017) studied the effects of initial solution pH on composition and morphology of nZVI corrosion products and selenium species in Se(IV)-nZVI reactions. Results showed that, under acid conditions, the reduction of Se(IV) was facilitated via thinning the iron oxide layer and further promoting the electron transfer from Fe° core to Se(IV). Furthermore, the amorphous FeOOH layer of fresh nZVI was observed to

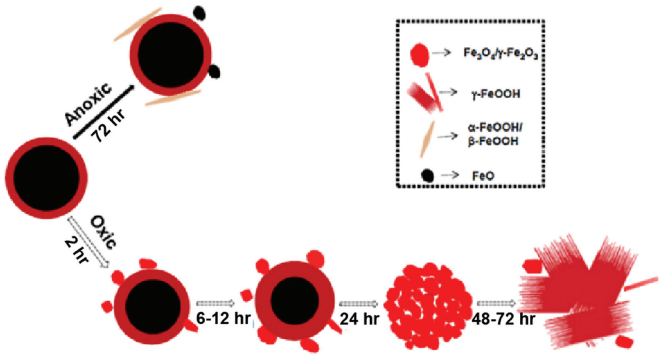

Fig. 2 – A conceptual model on nZVI evolution in water. Adapted with permission from (Liu et al., 2017).

be gradually corroded and recrystallized to form Fe_3O_4 crust, which served as a good conductor to further enhance the electron transfer for Se(IV) reduction. On the contrary, under alkaline and neutral condition, the oxidized iron formed anionic hydroxo species, such as $Fe(OH)_y^{2-y}$ or $Fe(OH)_x^{3-x}$. A passive layer of $Fe(OH)_2$(s) was therefore formed by precipitating these species. As the reaction proceeded, in the absence of oxygen, $Fe(OH)_2$(s) was oxidized to thicker plates of green rust and continuously transformed into smaller, thick crystals of Fe_3O_4. With the assistant of Fe_3O_4, the efficient electron transfer could be ensured even at heavy thickness of outer layer. As a consequence, the reduction of Se(IV) to Se(0) was also achieved at high pH. Wu et al. (2017b) also investigated the influence mechanism of pH on iron corrosion in As(V)-nZVI reaction. Although the phase of iron corrosion products was not obviously affected by pH value, the proportion of the γ-FeOOH decreased as well as Fe_3O_4/γ-Fe_2O_3 enhanced with the increasing pH value. Since Fe_3O_4/γ-Fe_2O_3 performed a stronger affinity for As(V) adsorption, the immobilization of As(V) with nZVI was favored under alkaline conditions. On the whole, difference in initial pH would influence the types of iron corrosion products or their proportion. As mentioned before, the corrosion products do pose significant impact on the contaminant removal capacity of nZVI, since they can act as intermediates for electron transfer as well as sorptive sites for decontamination.

2.1.3. *Coexisting anions and cations*

Some coexisting anions (e.g., NO_3^-, Cl^-, SO_4^{2-}, HPO_4^{2-}, HCO_3^-) may exhibit promotive or inhibitive effects on nZVI corrosion in aqueous solution to various degrees. In particular, the corrosion of nZVI promoted by NO_3^- was mainly manifested in the competition between NO_3^- and other pollutants on nZVI surface active sites and the corrosion of nZVI surface oxide layer (Liu et al., 2012). Due to the pitting effect (Yang et al., 2021), both Cl^- and SO_4^{2-} could aggregate the corrosion of nZVI by destroying the passivation layer of nZVI. The iron minerals produced were similar, which were magnetite/maghemite, lepidolite and goethite (Pullin et al., 2017a). Corrosion of nZVI in HPO_4^{2-} solution led to the formation of a small amount of iron oxide and phosphate mineral phase ($Fe_4(PO_4)_2OH_6 \bullet xH_2O$). At the same time, phosphate would cause not only chemical precipitation of the self-corrosion products with particles in the aqueous phase, but also co-precipitation with $Fe(OH)_2$ and $Fe(OH)_3$ to form the passivation layer of iron mineralization, which blocked the formation of the active sites, thus reducing the corrosion degree of nZVI (Wen et al., 2014). In the HCO_3^- solution, aging nZVI kept intact core–shell structure, but the shell experienced dissolving with surface cracks and shape deformation (Hua et al., 2018b).

In addition to common anions, coexisting cations also affect the corrosion behavior of nZVI in aqueous solutions. According to some studies, cations, such as such as Ca^{2+} and Mg^{2+}, have been shown to co-precipitate with dissolved iron ions to form iron surface complexes, which lead to surface passivation (He et al., 2016b; Xin et al., 2016).

2.1.4. *NOM*

In natural aquatic environments, the prevalent presence of NOM such as humic acid (HA) may pose a significant impact on the reaction activity and long-term performance of nZVI. NOM contains many functional groups, such as hydroxyl, carboxyl and phenolic groups, which could combine with Fe^{2+} and Fe^{3+} to form organometrical chelates, thereby inhibiting the corrosion of nZVI and reducing the conversion of Fe^0 to other mineral phases (Lv et al., 2013). Kim et al. (2018) observed that the reactive Fe^0 content of nZVI after 30 days of aging in HA solution was 61.6%, which was nearly 1.5-fold higher than that of nZVI in deionized water. The corrosion products were mainly hematite. It could be explained that the complexation of HA and nZVI produced aromatic/hydrophobic moieties on the surface, which hindered the electron transfer between nZVI and water, so as to alleviate the oxidation of nZVI by water. Further study showed that, the corrosion degree of nZVI was similar regardless of the presence of oxygen in HA solution, indicating that HA could protect nZVI from oxidation of dissolved oxygen. However, another study reported that the corrosion of nZVI coated with polyacrylic acid was accelerated by HA, leading to the cubic magnetite production (Kim et al., 2014). The different conclusions may be ascribed to the nZVI modification and different reaction conditions. To date, researches put a great deal of efforts into understanding the effects of HA, unfortunately, ignoring how other types of NOM may influence the corrosion behavior of nZVI.

2.2. Corrosion of modified nZVI

Poor stability and unsatisfactory reactive lifetime of iron nanoparticles are salient questions for successful applications of nZVI technology. Therefore, prior and ongoing researches have focused on the nZVI modification, including surface stabilizer coating, bimetal decoration, and sulfidation treatment. The variations in the physiochemical properties of nZVI may result in the different corrosion behaviors.

2.2.1. Polymer-stabilized nZVI

Bare (unmodified) nZVI particles are particularly prone to aggregation due to chemical and magnetic interactions (Phenrat et al., 2007). A popular method to improve their unsatisfactory colloid stability and transportability is coating with polymer stabilizers, such as caboxymethyl cellulose (CMC), polyacrylamide (PAM), poly styrene sulfonate (PSS) and poly acrylic acid (PAA).

Liu et al. (2016) found that after anionic PAM (APAM) and CMC modification, a thin film was formed onto the nZVI surface. This film could protect zero-valent iron from aggressive corrosion, since after 2 hr oxidation in water, there were little flaky-structured iron oxides generated for polyelectrolyte-modified nZVI while numerous flakes were observed onto the surface of pristine-nZVI. Dong et al. (2017, 2016) further studied the evolution of CMC modified nZVI after long-term exposure to static water and simulated groundwater. The results showed that CMC modification not only affected nZVI aging process, but also influenced the corrosion products. After CMC coating, the oxidation rate of nZVI slowed down. In particular, after 90 days of aging in static water, the main corrosion products were not Fe_3O_4/Fe_2O_3, but γ-FeOOH. Moreover, γ-FeOOH was found to be more abundant with increasing loading of CMC.

2.2.2. Bimetallic nZVI

To catalytically enhance the reactivity of nZVI toward organic pollutants, bimetallic nZVI has been fabricated. Metal catalysts (e.g., Pd, Pt, Ni, and Cu) with more positive standard reduction potential than that of Fe° can be reduced by nZVI to form metallic nanoparticles onto the nZVI surface. A growing body of evidence has proved that doping a second metal can effectively improve the nZVI decontamination capacity and help generate more benign end-products in the reductive dehalogenation of organic halides. Meanwhile, due to the galvanic effects, nZVI will undergo more prominent structural and morphological changes, which are induced by accelerated iron corrosion.

Yan et al. (2010b) employed aberration-corrected scanning transmission electron microscopy coupled with energy-dispersive X-ray spectroscopy (STEM-XEDS) to track the evolution of Pd-nZVI in an aqueous environment. Freshly prepared Pd-nZVI particles displayed a rough surface profile with discrete Pd nanoclusters (2–5 nm in size). After 24 hr aging, the Pd penetrated through the iron oxide outerlayer toward the iron core and accumulated as a buried layer at the metallic Fe/oxide interface. In the meantime, the metallic iron diffused outward, oxidized, and contributed to the FeOOH external shell until all the metallic iron was exhausted. The XPS analysis further confirmed that the Pd-nZVI experienced a more severe oxidation than pristine nZVI. Dong et al. (2018a) carried out in-depth research on the physicochemical transformation of Ni-nZVI in simulated groundwater. After a 5-day short-term aging period, the corrosion of Ni-nZVI in simulated groundwater occurred rapidly (within hours) and transformed to Fe^{2+}, indicating the rapid loss of electrons from iron core. After long term aging (up to 90 days), the spherical iron particles evolved into larger-sized rod-, sheet-, and needle-like oxides, which were denoted as Fe_3O_4 and γ-Fe_2O_3. Additionally, during the corrosion process, most of Ni on the surface of Ni-nZVI particles were encapsulated by the iron oxides with trace amount of Ni releasing into solution.

2.2.3. Sulfidated nZVI (S-nZVI)

S-nZVI, produced from the reaction of nZVI with sulfide precursors, possesses a unique nanostructure with sulfur not only incorporated onto the surface but also into Fe^0 BCC matrix (Su et al., 2018; Xu et al., 2020b). It has attracted great interest as it can inhibit reactions with water and enhance the reactivity and selectivity for target contaminants (Garcia et al., 2021; Zhang et al., 2020). Emerging studies suggest that the mechanisms responsible for this enhancement are electron transfer control, higher hydrophobicity, and abundant reactive sites provided by sulfidation (Li et al., 2017b; Xu et al., 2020a, 2020b). Given that, researchers investigate the corrosion process of S-nZVI to clarify whether and how sulfidation influence the longevity of iron nanoparticles.

According to recent studies, specific corrosion behaviors of S-nZVI are mainly dependent on sulfidation procedures (e.g., co-sulfidation (S-nZVIco), post-sulfidation (S-nZVIpost)), as well as aquatic environment conditions. Xiao et al. (2022) systematically compared the aging process of S-nZVIco and S-nZVIpost in anaerobic simulated groundwater. After 60–90 days' aging, both S-nZVIco and S-nZVIpost produced flaky and needle-like iron corrosion products. Nevertheless, there was a substantial difference between S-nZVIco and S-nZVIpost in terms of the diffusion directions of corrosion regions. That was, for corroded S-nZVIco, the corrosion zones progressed from the edge of the core toward the center, resulting in a concentric structure and the destruction of the spherical shapes of some particles; however, for corroded S-nZVIpost, due to Kirkendall effect, a hollow structure formed as corrosion regions outward from the core center. It was assumed that the discrepancy of the sulfur distribution resulted from different sulfidation procedures might explain this interesting difference in corrosion phenomena. Similar finding was also reported in another study. Mangayayam et al. (2019) visualized the progressive compositional change and structural transformation of S-nZVIpost in anoxic artificial groundwater. From day 10 to 60, molar fraction of Fe^0 decreased to about 50% of its initial amount; from day 60 to 120, only slight additional corrosion occurred. By contrast, corrosion of nZVI started instantly, with almost 80% of Fe^0 oxidized after 60 days. Up to 180 days, TEM imaging and EDX elemental mapping of spent S-nZVI also depicted an analogous "hollow" core surrounded by an intact mackinawite-like shell, indicating the significant oxidation of iron core. The main corrosion products were hexagonal crystal platelets of micron-sized, which were found to be green rust (GR_{CO_3}). In addition to anaerobic artificial groundwater, the transformation of S-nZVI over time in

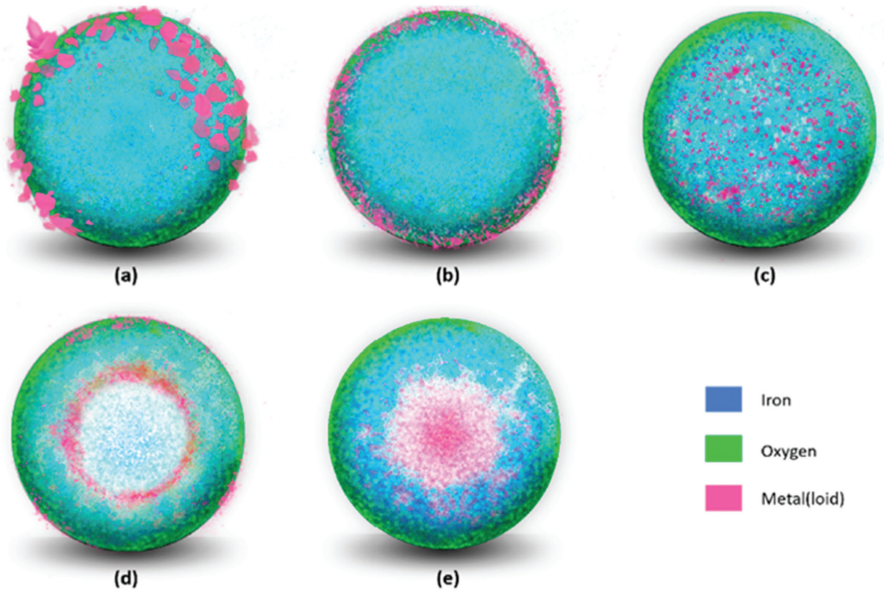

Fig. 3 – Architectural corrosion of metal(loid)s-bearing nZVI (a, seed; b, subshell; c, spot; d, hollowshell; e, U-yolk). Adapted with permission from (Li et al., 2021a; Ling and Zhang, 2015).

deoxygenated deionized water was also identified (Dong et al., 2018b). Over an aging period of 30 days, the corrosion products were iron (hydr)oxides (e.g., γ-FeOOH and Fe_3O_4/γ-Fe_2O_3) and iron sulfide (e.g., FeS, FeS_2, and Fe_3S_4). Interestingly, XRD patterns revealed that with increasing aging time, the peaks assigned to iron sulfide became more evident. Taken together, sulfidation of nZVI do effectively protect the iron nanoparticles from aggressive corrosion and prolong its reactive lifetime.

2.3. *Corrosion of metal(loid)s-bearing nZVI*

Core–shell structured nZVI stands out with its fascinating chemistry and multiple functionalities for contaminants transformation and separation, especially for the sequestration or recovery of heavy metals from water. As shown in Fig. 3, researchers, especially Zhang and Ling's group, have made great efforts on studying the metal(loid)s-nZVI solid-phase reactions and heterostructures formed from corrosion at near-atomic resolution (Hua et al., 2018a; Li et al., 2021a; Ling et al., 2018a; Ling and Zhang, 2015). For metal cations, including Ag(I), Cu(II), Au(III) with high redox potential, the formation of numerous galvanic couples improves the electron tunnel from the iron core, resulting in the intense corrosion of nZVI, as well as the immediate emergence of a zero-valent "seed" and "dendrite" (i.e., Ag^0, Cu^0 and Au^0) on the iron oxide shell by direct reduction (Ling et al., 2018a, 2018b, 2017; Yan et al., 2010b). For the electronegative oxyanion metalloids, including As(III)/As(V) and Se(VI), they preferentially experience the following procedure: (i) attraction and chemical binding of the metalloid in solution on the oxide shell; (ii) reduction of the adsorbed metalloid; (iii) diffusion of the reduced metalloid across the defects of oxide layer and further formation of metalloid "subshell" at the subsurface of the iron nanoparticle (Ling et al., 2015; Ling and Zhang, 2014a, 2017; Liu et al., 2018; Tang et al., 2021). For the metal cations such as Zn(II) and Cs(I) with low redox potential, the spent nZVI maintains a comparably intact "core–shell" structure with sorption or surface complexation of Zn(II) and Cs(I) on the iron oxide shell (Ling et al., 2017). Interestingly, for the paramagnetic metal ions such as Co(II) and Ni(II), powered by Kirkendall effect, the Fe° core has been completely consumed, leaving only a doughnut-like or horseshoe (half-doughnut)-like structure, with large cavities at inner region (Ling and Zhang, 2014b). For the radioactive U(VI), it could be enriched and encapsulated in the core of the iron nanoparticles to form a yolk-like structure (Ling and Zhang, 2015).

In addition to the inherent character, the different concentrations of metal(loid)s in the solution make the morphology and structure of corrosion products vary greatly after the reaction. For instance (Huang et al., 2018), in low Cr(VI) concentration (10 mg/L) and under anaerobic conditions, the surface of nZVI particles became rough after corrosion, with the regular spherical surface obvious collapse. On the contrary, in high concentration (100 mg/L) and under anaerobic conditions, the high level of Cr(VI) was reduced to Cr(III) by Fe° core, while Fe^0 was oxidized to Fe(II)/Fe(III), forming Fe(III)-Cr(III) passivation layer on the particle surface. Insoluble and insulation of Fe(III)-Cr(III) (oxy)hydroxide layer could completely covered in nZVI surface layer, shielding electron transfer. In other words, this double layer structure possessed excellent corrosion resistance, so the resulted particles were spherical, kept "core–shell structure".

In a word, driven by the standard redox potential E^0 between iron and metal(loid), the Kirkendall effect, the properties of metal(loid)s (e.g., magnetic property, electrical charge and conductivity), as well as the solution chemistry (e.g., metal(loid) concentration), geometries and

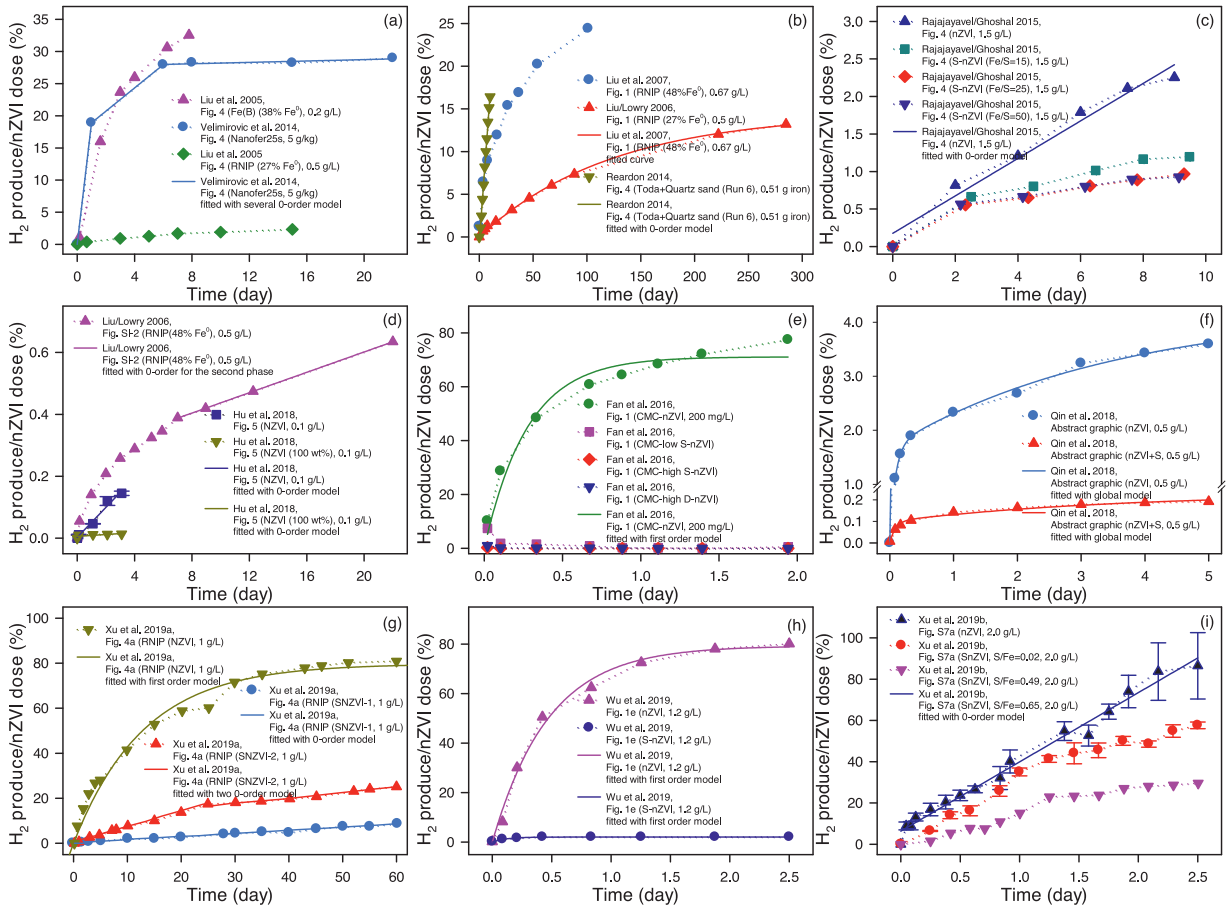

Fig. 4 – Summary of H_2 kinetic data in nZVI/H_2O corrosion system from previously published research (Fan et al., 2016; Hu et al., 2018; Liu et al., 2007, 2005; Liu and Lowry, 2006; Qin et al., 2018; Rajajayavel and Ghoshal, 2015; Reardon, 2014; Velimirovic et al., 2014; Wu et al., 2019; Xu et al., 2019a, 2019b). The solid lines replicate the modeling results given in the original papers where the data were first reported.

growths of iron corrosion products can be tuned (Li et al., 2021a).

3. Corrosion kinetics of nZVI in water

Since the corrosion process is dynamic, the establishment of time-resolved methodologies to monitor iron corrosion is required. In this section, common analytical technologies, including hydrogen evolution measurement, mass characterization, energy spectrum analysis, chemical redox probe and electrochemical characterization, are introduced for building corrosion kinetics model.

3.1. *Hydrogen evolution measurement*

A particularly important process during nZVI corrosion is reaction with water to produce H_2, commonly known as hydrogen evolution (HER) (Qin et al., 2018). Hydrogen generated by nZVI corrosion is a potential electronic resource. In groundwater remediation, hydrogen generated can be used by H_2-utilizing bacteria for biodegradation, or can escape from groundwater as a separate gas phase (Reardon, 2014).

The formation of H_2 is a relatively direct and effective method to determine the reactivity of nZVI. Scholars calculate the corrosion rate of nZVI via monitoring the hydrogen production process, thus determining the content of iron in nZVI (Fan et al., 2016; Velimirovic et al., 2014). In the process of contaminants degradation, the evolution of hydrogen cannot be ignored as well. For instance, the rate of dechlorination of trichloroethylene (TCE) depends on the rate of hydrogen generated by iron corrosion (Liu and Lowry, 2006). In addition, according to chemical equations and stoichiometry, the generation of hydrogen can be measured to find out the recipients of nZVI electrons.

Many scholars have determined the generated hydrogen under anaerobic conditions and fitted its kinetics according to the release law, as shown in Fig. 4 and Table 1. The kinetic fitting equations of hydrogen can be divided into three categories: zero-order, first-order, zero-order and first-order combination. Different time scales, experimental conditions, nZVI samples and the treatment of samples will correspond to different kinetics fitting equations, as well as different corrosion rate constants calculated. From the data, the corrosion rate constants were basically the same order of magnitude. The first set had a rate constant of 31.0 μmol L g^{-1} hr^{-1}, several

Table 1 – Summary of the corrosion kinetics of nZVI from different origins.

Origins of nZVI	Treatment	Reaction conditions	Kinetic model	Rate constant	Refs.
$Fe^{H2(D)}$	None	DO/DI water 0.033 g/L	Zero-order	1.1719–6.7396 μmol $L{\cdot}g^{-1}{\cdot}hr^{-1}$	(Sarathy et al., 2008)
$Fe^{H2(W)}$		0.017 g/L		0.1563 μmol $L{\cdot}g^{-1}{\cdot}hr^{-1}$	
Toda	None	quartz, $H_2O_{(l)}$, $H_2O_{(g)}$ 3.2 kPa	Zero-order	0.5142 μmol $L{\cdot}g^{-1}{\cdot}hr^{-1}$	(Reardon, 2014, p.)
Nanofer25s	None	Synthetic groundwater 5.150 g/L	Zero-order	0.4229 μmol $L{\cdot}g^{-1}{\cdot}hr^{-1}$	(Velimirovic et al., 2014)
RNIP		4.740 g/L		0.0884 μmol $L{\cdot}g^{-1}{\cdot}hr^{-1}$	
Fe/B	None S/Fe=5.4 ± 0.5 mol %[a] S/Fe=0.8 ±0.1 mol %[b]	DO/DI water pH_{ini} =6.0 rotator at 30 r/min at 22 ± 2 °C 1 g/L	Zero-order	2.8358 μmol $L{\cdot}g^{-1}{\cdot}hr^{-1}$ 0.0853 μmol $L{\cdot}g^{-1}{\cdot}hr^{-1}$ 0.4715 μmol $L{\cdot}g^{-1}{\cdot}hr^{-1}$	(Xu et al., 2019b)
Fe/B	None 10∼100 wt.% $Mg(OH)_2$	$[NaHCO_3]$=1.0 mmol/L 0.1 g/L N_2	First-order	2.7560 μmol $L{\cdot}g^{-1}{\cdot}hr^{-1}$ 0.0815–2.2143 μmol $L{\cdot}g^{-1}{\cdot}hr^{-1}$	(Hu et al., 2018)
Fe/B	None (S/Fe=0.02-0.09)[b] CMC-nZVI (S/Fe=0.05) nZVI/Pd (Pd/Fe=0.5 wt.%)	orbital shaker at 300 r/min at 22 ± 2 °C	First-order	0.0060 $L{\cdot}g^{-1}{\cdot}hr^{-1}$ 0.0675–0.2175 $L{\cdot}g^{-1}{\cdot}hr^{-1}$ 0.2150 $L{\cdot}g^{-1}{\cdot}hr^{-1}$ 12.2 $L{\cdot}g^{-1}{\cdot}hr^{-1}$	(Rajajayavel and Ghoshal, 2015)
Fe/B	CMC-nZVI (CMC 0.5 wt.%)	DO/DI water 0.2 g/L N_2	First-order	0.3335 $L{\cdot}g^{-1}{\cdot}hr^{-1}$	(Fan et al., 2016)
Toda	None S/Fe=0.34–2.02[b]	pH_{ini} =7.0 (buffer) 0.5 g/L	First-order	0.0446 $L{\cdot}g^{-1}{\cdot}hr^{-1}$	(Qin et al., 2018)
CMC-nZVI	None S/Fe=0.34–1.01[b]	N_2		0.2734 $L{\cdot}g^{-1}{\cdot}hr^{-1}$	
Toda	None S/Fe=0.34–2.02[b]	pH_{ini}=7.0 (buffer) 0.5 g/L	Zero-first-order	0.0594 $L{\cdot}g^{-1}{\cdot}hr^{-1}$	
CMC-nZVI	None S/Fe=0.34–1.01[b]	N_2		0.6978 $L{\cdot}g^{-1}{\cdot}hr^{-1}$	
Toda	None S/Fe=0.34–2.02[b]	pH_{ini}=7.0 (buffer) 0.5 g/L	Three First-order	0.1256 $L{\cdot}g^{-1}{\cdot}hr^{-1}$ (k_1) 0.0302 $L{\cdot}g^{-1}{\cdot}hr^{-1}$ (k_2)	
CMC-nZVI	None S/Fe=0.34–1.01[b]	N_2		0.9620 $L{\cdot}g^{-1}{\cdot}hr^{-1}$ (k_1) 0.0230 $L{\cdot}g^{-1}{\cdot}hr^{-1}$ (k_2)	
Toda	None S/Fe=0.34–2.02[b]	pH_{ini}=7.0 (buffer) 0.5 g/L	First-/First-order	0.0716 $L{\cdot}g^{-1}{\cdot}hr^{-1}$ (k_1) 0.0108 $L{\cdot}g^{-1}{\cdot}hr^{-1}$ (k_2)	
CMC-nZVI	None S/Fe=0.34–1.01[b]	N_2		0.9676 $L{\cdot}g^{-1}{\cdot}hr^{-1}$ (k_1) 0.0234 $L{\cdot}g^{-1}{\cdot}hr^{-1}$ (k_2)	
Fe/B	$[S/Fe]_{particle}$=0–1.13 mol%[b]	rotator at 30 r/min at 22 ± 2°C DO/DI water pH_{ini}=6.0 2.0 g/L	First-order	0.0001–0.0004 $L{\cdot}g^{-1}{\cdot}hr^{-1}$	(Xu et al., 2019a)
CMC-nZVI	None	ethanol/water 500 μL/min	Exponential-logarithmic	0.0060–0.0480 hr^{-1} (k_1) 0.0222–0.1210 (k_2)	(Greenlee et al., 2012)
Fe/B	Ni/Fe=0–0.005	50 μL/min		1.14–15.36 hr^{-1} (k_1) 0.0142–0.0251 (k_2)	

[a] represents the S-nZVI-1, which was synthesized with one-step method.
[b] represents the S-nZVI-2, which was synthesized with two-step method.

times larger than others. And it could be explained that the rate of hydrogen evolution was the greatest at the first day of corrosion (Liu et al., 2005). Overall, these reports data were similar. In particular, Qin et al. (2018) studied four kinetic models at the same time and determined the best kinetic model by global fitting. The research showed that model 4 could primely describe complex systems and was applicable to various diagnostics and predictions.

According to the collected data, the zero-order model is simple to fit and conforms to the linear law. However, in some reactions, the zero-order model can only fit a certain stage and does not conform to the overall data (Liu et al., 2005). The first-order model is also relatively simple and sometimes deviates from the actual data, but it can still accurately describe the corrosion kinetics (Fan et al., 2016). The combination of the two first-order models used in global fitting is complex, taking multiple factors into account, such as two reaction phases. Although the global fitting analysis can be carried out for all data, it is not applicable for a long-period investigation and only suitable in the buffer system, which will be affected by other side processes when applied to the field conditions (Qin et al., 2018).

3.2. *Mass characterization*

Corrosion of nZVI will result in the escape of hydrogen, as well as the generation of new substances such as iron hydroxide and iron oxide, thus leading to mass change (Liu et al.,

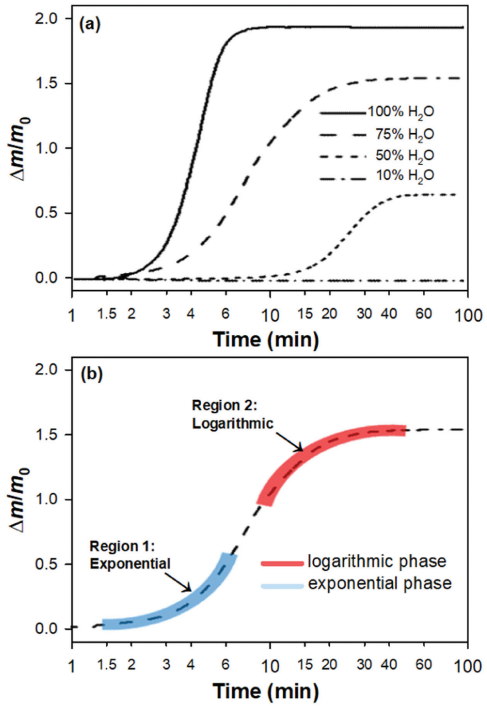

Fig. 5 – QCM analysis and model establishment of carboxymethyl cellulose nZVI (CMC-nZVI). CMC-nZVI at different H_2O/ethanol rations (Greenlee et al., 2012).

2017; Pullin et al., 2017b; Torrey et al., 2015a). However, in the aqueous phase, nZVI reacts very quickly, so there are few studies concerning the corrosion behavior by monitoring its mass. In recent years, quartz crystal microbalance (QCM) has been introduced to study the corrosion kinetics of nZVI (Gankanda et al., 2019; Greenlee et al., 2012). QCM is a precise technique for measuring mass change (Ma et al., 2008). Since Sauerbrey (1959) published his paper in 1959, QCM has been widely used in the study of adsorption kinetics and thin films growth kinetics (Ma et al., 2008; Okur et al., 2010; Ortega-Borges and Lincot, 1993; Qiu et al., 2011). In the rapid reaction of nZVI, QCM can obtain the mass change accurately and acutely via recording the frequency change (Torrey et al., 2015a). QCM continuously monitors mass change and further provides important and valuable information to study the reactions of nanoparticles (Torrey et al., 2015b). Therefore, the corrosion rate of nZVI can be determined by measuring the mass change and establishing the kinetic model.

As shown in Fig. 5, Greenlee et al. (2012) analyzed the quartz crystal microbalance monitoring data and found that the nZVI oxidation curve was divided into two regions. The first region, with exponential growth, indicated a surface-dominated oxidation controlled by migration of species (H_2O and O_2) to the surface. The second region of logarithmic increase was dominated by movement of species (e.g., iron cations and oxygen anions) through the oxide layer. Although other side processes inevitably occurred during the QCM experiment, such as iron dissolution, agglomeration, and water adsorption, which might slightly influence the mass measurements, it was believed that the kinetic model could still describe the possible oxidation mechanisms of nZVI. Gankanda et al. (2019) studied the effects of different ligands on the adsorption and oxidation behavior of nZVI. They focused on the adsorption kinetics, which was complementary to Greenlee's data. Noticeably, their experiments all found that the mass gain of nZVI was changed under the influence of different ligands, indicating that ligands would affect the oxidation kinetics of nZVI, which was of great significance for the practical application of nZVI synthesized with different stabilizer.

Unfortunately, QCM does not effectively distinguish between adsorption and oxidation processes. For example, Greenlee et al. (2012) used the QCM monitoring data to perform kinetic fitting on the premise that the SEM and XRD data showed that the oxidation product of nZVI in aerobic water was only iron hydroxide. However, the oxidation products of nZVI are rarely simple, and the oxidation products will change over time. In addition, the complex properties of natural water and the flow rate of water may also affect the oxidation kinetics of nZVI, so it is necessary to research further if this model can be applied to practical water treatment.

3.3. *Energy spectrum analysis*

Energy spectrum analysis can provide powerful evidence for the study of the structure and composition of nZVI corrosion products.

Mössbauer spectroscopy is a unique analytical tool for identification and quantification of the solid nZVI reaction species (Filip et al., 2014; Klimkova et al., 2011). Filip et al. (2014) studied the corrosion products of nZVI at 25 and 80°C in anaerobic conditions in detail. After sorting out the Mössbauer spectrum, time evolution of Mössbauer spectral areas corresponding to nZVI and $Fe(OH)_2$ during corrosion reaction was illustrated (Fig. 6a, b). Studies showed that $Fe(OH)_2$ was the only corrosion product of nZVI under the anaerobic condition at 25°C. However, when the temperature rose to 80°C, the metastable $Fe(OH)_2$ gradually transformed into stable Fe_3O_4. The reaction of nZVI with water under anaerobic condition was further analyzed quantitatively with Mössbauer spectrum. The data conformed to the pseudo-first-order kinetic equation, specifically, the reaction rate constants of nZVI and water under the conditions of 25°C and 80°C were 1.14×10^{-3} hr^{-1}($\pm 3.6 \times 10^{-5}$) and 6.8×10^{-3} hr^{-1}($\pm 1.4 \times 10^{-3}$), respectively.

The extended X-ray absorption fine structure (EXAFS) can offer quantitative information about the types and proportions of iron species (He et al., 2016a; Reinsch et al., 2010). For instance, Fe K-edge EXAFS was used to study the solid phase of Fe species in nZVI under aerobic conditions. Linear combination fits (LCF) of the K^3-weighted EXAFS spectra indicated that after exposure to oxygenated water, nZVI first transformed to ferrihydrite and then lepidocrocite (Fig. 6c). The transformation of each mineral phase could be quantified by the first-order kinetic fitting. According to the kinetic calculation, two rate constants were obtained: k_1=6.1 $\times$ 10^{-3} sec^{-1}(transformation between nZVI and ferrihydrite), k_2=1.14 $\times$ 10^{-3} hr^{-1}(transformation from ferrihydrite to lepidocrocite).

XRD is mainly used to identify the bulk chemical compositions of the mineral, and analyze the changes of the sam-

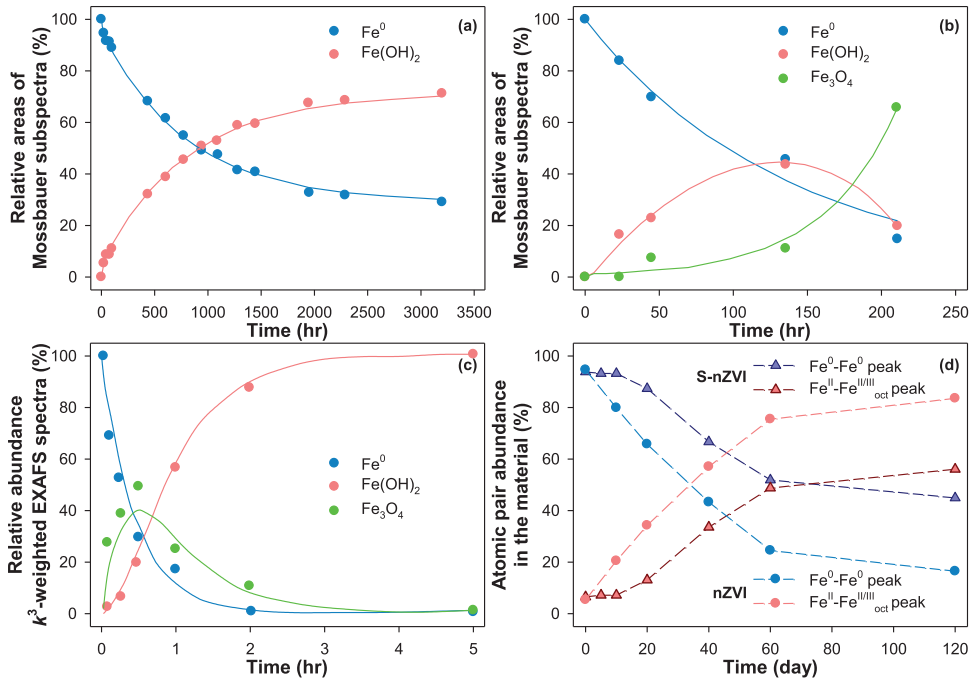

Fig. 6 – Time evolution of Mössbauer spectral areas corresponding to anaerobic reaction of nZVI with water at (a) 25°C and (b) 80°C; (c) Transformation of solid phase Fe speciation during 5 hr exposure to oxygenated water; (d) Changes in structure and composition of nZVI and S-nZVI continuously exposed to anoxic artificial groundwater (Chekli et al., 2016; Filip et al., 2014; He et al., 2016a; Klimkova et al., 2011; Mangayayam et al., 2019; Reinsch et al., 2010).

ple before and after the reaction (Bae et al., 2018; Chekli et al., 2016). If the structures of the material and its phase compositions need to be further quantitatively analyzed, other technical supports are required, such as pair distribution function (PDF) analyses and Rietveld refinement (Chekli et al., 2016; Mangayayam et al., 2019). Mangayayam et al. (2019) used XRD and PDF to analyze the bulk structure of nZVI corrosion in anoxic artificial groundwater. Results showed that with the increase of time, Fe^0–Fe^0 atomic pair abundance decreased, but the Fe^{II}–Fe^{III} atomic pair abundance increased (Fig. 6d). Moreover, the abundance of the two atomic pairs corresponded to the decrease of Fe cores and the increase of green rust and white rust (WR). The sulfidized nZVI (S-nZVI) corroded more slowly than the untreated nZVI, and about 80% of the Fe^0 was oxidized after 60 days, indicating that under anaerobic condition, sulfidation could indeed inhibit the side reaction with water (Mangayayam et al., 2019; Rajajayavel and Ghoshal, 2015).

With comprehensive characterization capacity, energy spectrum analysis offers a viable option to qualitative and quantitative monitor of reaction kinetics and reaction mechanism, which can deep our understanding of nZVI corrosion in water. Specifically, the quantification of corrosion behavior of nZVI in water can be achieved by spectrum and supplemented by numerical calculation to obtain the corrosion rate constant.

3.4. *Chemical redox probe*

Chemical redox probe is an intuitive method for fast diagnose of redox conditions, which can be utilized to investigate nZVI corrosion behavior in water directly (Shi et al., 2015). Redox activity indicators such as indigo-5,5'-disulfonate (I2S) have long been utilized to characterize the redox properties in environmental chemical systems (Jones, 2001; Li et al., 2017a; Tratnyek et al., 2001). When redox dyes are used as probe compounds, the probe response is characterized by color changes, which are distinguished by the color differences between the oxidation state and the reduced state of the probe compounds. These color changes can be quantified by common methods such as spectrophotometry. Some redox probes have fluorescence spectra, and the measured data can be used to characterize the thermodynamic and kinetic characteristics of reaction systems (Johnson et al., 2013; Tratnyek et al., 2001).

Shi et al. (2015) used I2S as a chemical redox probe to characterize the fate and effects of nZVI during groundwater remediation. In the kinetics experiment, I2S was added to a solution with a total iron concentration of 10 mg/L (a mixture of carboxymethyl cellulose nZVI (CMC-nZVI) and Fe^{2+} solutions in different quantities). According to the observation of the absorbance at 610 nm, it could be seen from Fig. 7 that the reduction of I2S by Fe^{2+} aqueous solution was not obvious. However, with the increase of CMC-nZVI concentration, the platform absorbance decreased, indicating that the total reduction amount of I2S increased. Therefore, the selectivity of I2S to Fe^0 renders it a promising method to distinguish between Fe^0 and aqueous Fe(II), which is difficult to be identified by other measurements. Fan et al. (2015) conducted an in-depth field study on the application of I2S on their preliminary work, in which I2S was used as a chemical redox probe to characterize nZVI reactivity and transformations. The CMC-nZVI with concentration of 2 and 4 mg/L was fitted by the second-order kinetic model. The model is robust enough to describe

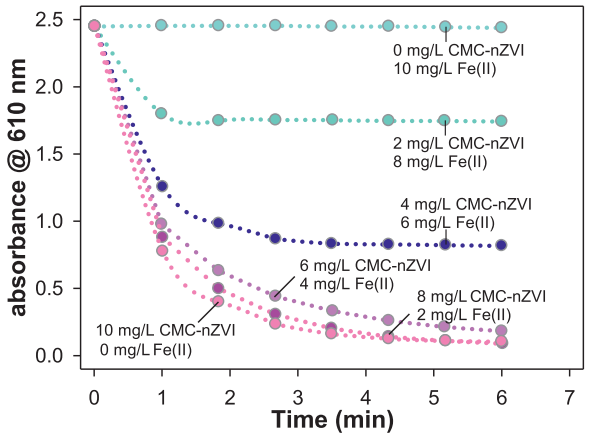

Fig. 7 – Reduction kinetics of indigo disulfonate (I2S) by mixtures composed of different amounts of CMC–nZVI and aqueous Fe(II) with 10 mg/L total iron concentration (Shi et al., 2015).

both fresh and aged samples, which is a practical method for field characterization of nZVI. However, it is only applicable to the case of complete consumption of nZVI. Besides, since I2S will be reoxidized in exposed air after reduction by nZVI, this method is only suitable for anoxic and anaerobic conditions, which cannot model the reactivity and transformation of nZVI under aerobic condition.

3.5. *Electrochemical characterization*

Since the corrosion behavior of nZVI in aqueous solution is dynamic and ongoing, the growing importance of the *in situ* and real-time electrochemical technology is thus highlighted. The electrochemical model can directly monitor and control the redox reaction of Fe^0–water interface. Thus, it has always been used to study the redox reaction and corrosion resistance of nZVI in solution (Nurmi and Tratnyek, 2008; Qi et al., 2019; Sarathy et al., 2008; Turcio-Ortega et al., 2012).

Among common electrochemical characterization methods, the open circuit potential measured by powder disk space (PDE) is a mixed potential, reflecting the equilibrium potential of the dominant redox couples, that is, the equilibrium potential of Fe corroded by H_2O (Tratnyek et al., 2011; Xu et al., 2019a). Open circuit potential (OCP) represents the corrosion tendency of iron. Specifically, the more negative OCP indicates greater iron corrosion tendency (Xu et al., 2019a). Hence, OCPs can be used as a sensitive indicator to provide real-time data support for the changes of redox reactions on the surface of the materials.

OCP is continuously changing, which can be monitored for a long time to grasp the redox reaction of the material in this period of time as a whole. Turcio-Ortega and Xu's teams monitored the reactivity of nZVI and S-nZVI in water using OCP. Turcio-Ortega et al. (2012) studied the redox properties of nZVI and S-nZVI in deoxy/deionized (DO/DI) water, background ion solution, and buffer solution, respectively (Fig. 8). Compared with nZVI, S-nZVI was more stable in the three solutions. In DO/DI water, the open circuit potential of nZVI became more negative within 1 hr, decreasing about 0.05 V, while the open circuit potential of S-nZVI increased slightly, indicating that sulfidation did inhibit the reaction between nZVI and water (Fig. 8a). In the solution containing Cl^- of 0.01 mol/L, the open circuit potential of S-nZVI decreased significantly, indicating that Cl^- made it easier to break through its passivation film thus affect depassivation. In TRIS buffer (prepared from tris(hydroxymethyl)-aminomethane) with pH=7.5, the open circuit potentials of the two nanoparticles were not significantly different. In addition, in order to study long-term effects, the open circuit potential of 4 days was recorded in the aeration of 0.1 mol/L NaCl solution, and the open circuit potential rebounded after aeration, possibly due to the formation of passivation film again (Fig. 8b, c).

Xu et al. (2019a) studied the effect of the ratio of different [S/Fe] on the reactivity of S-nZVI. The results showed that when the ratio of $[S/Fe]_{particle}$ was within the range of 0.02–0.65 mol%, the open circuit potential was more positive than that of nZVI, indicating that the corrosion tendency of nZVI in water was reduced by sulfidation. However, the initial OCP of the highest $[S/Fe]_{particle}$ (1.13 mol%) was more negative, indicating that the highest $[S/Fe]_{particle}$ enhanced the iron corrosion tendency, which might be ascribed to the surface of nZVI completely covered by sulfur, leading to the active site block, thus preventing the corrosion with water (Fig. 8d).

Shi et al. (2011) used a rotating disk electrodes (RDE) to monitor the nZVI oxidation-reduction potential (ORP), and studied the effect of rotational speed on ORP in two different buffer systems (Fig. 8e). All data showed that ORP could smoothly transform to a relatively stable value. At higher speeds, the transition period was even shorter. The value of ORP obtained at higher rotational speed was more negative, which might be attributed to the greater contact area between nZVI and the electrode surface, and/or the higher concentration of nZVI near the electrode.

In short, the electrochemical technology is a powerful tool to facilitate precise characterization of the redox reaction in nZVI-water interfaces. Understanding the electrochemical characteristics of nZVI in water will help us elucidate the more complex iron corrosion behavior at ever finer length scales.

To sum up, the respective focus and advantages and disadvantages of different characterization methods for studying the corrosion kinetics of nZVI in water are compared in Table 2. For example, the hydrogen evolution measurement and QCM analysis are powerful tools to study the corrosion kinetics in a single nZVI treatment system, however, they cannot be used to predict the corrosion behavior of nZVI precisely in the field application. Besides, the redox probe, which responds to color changes, is considered as a simple and fast analytical method to evaluate the transformation of nZVI intuitively with field practicability. Unfortunately, I2S will be oxidized and discolored immediately after contact with air, so it is only applicable to anaerobic conditions.

4. Conclusion and prospect

Nanoscale zero-valent iron (nZVI) is prevailing as a green agent for cost-effective contaminant transformation and separation. Although a lot of reviews are carried out on synthesis,

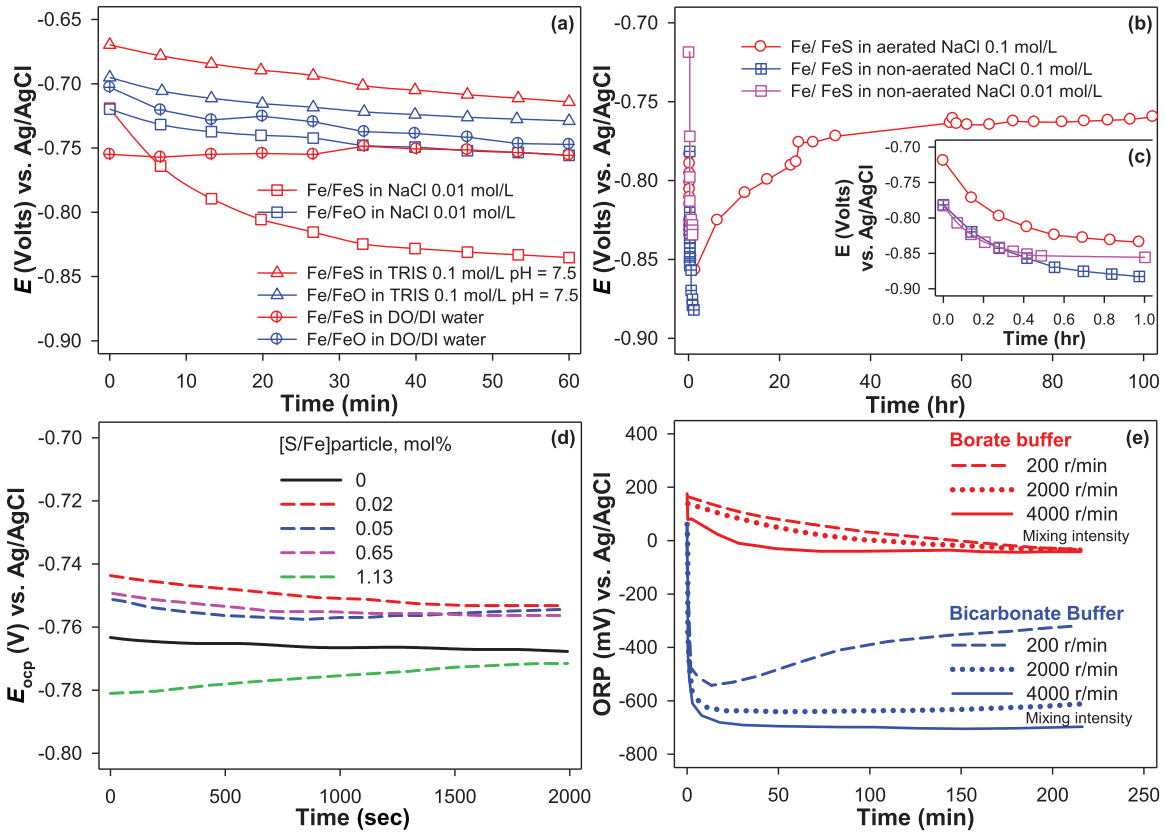

Fig. 8 – Open-circuit chronopotentiograms (CPs) and oxidation-reduction potential (ORP) for characterizing the nZVI corrosion in water (Shi et al., 2011; Turcio-Ortega et al., 2012; Xu et al., 2019a).

Table 2 – Overviews of the methods for studying the corrosion kinetics of nZVI in water.

Characterization Methods	Suitable occasions		Qualitative/semi-quantitative/quantitative	Obtained information
Laboratory/Field	with/without O_2			
H_2M	Laboratory	without	Quantitative	Kinetic
MC	Laboratory	with/without	Quantitative	Kinetic
ESA	Laboratory	with/without	Qualitative/Semi-quantitative	Behavior/Kinetic
CRP	Laboratory/Field	without	Qualitative/Quantitative	Kinetic
EC	Laboratory	with/without	Qualitative/Semi-quantitative/Quantitative	Behavior/Kinetic

Note: The H_2M, MC, ESA, CRP, and EC in the table stand for the H_2 measurement, mass characterization, energy spectrum analysis, chemical redox probe, and electrochemical characterization, respectively.

modification and characterization methods, decontamination performance, as well as field application investigation of nZVI, less attention has been paid to the overview on corrosion behaviors and kinetics of nZVI in water when determining the final state and fate of nZVI in the environment. In this article, Eh-pH diagram for predicting the thermodynamics trends of iron corrosion, corrosion behaviors of (modified-) nZVI under varied environmental conditions, and analytical methods and characterization technologies for establishing time-resolved corrosion kinetics are reviewed. Nevertheless, some efforts are still needed in future research and practical applications.

(i) The nZVI corrosion in natural systems is even more complex, since the reaction processes and the products are highly influenced by environmental physicochemical conditions, such as groundwater composition, water velocity, dissolved oxygen, temperature, pH, redox potential and alkalinity. Thus, the nZVI corrosion kinetics obtained under laboratory conditions are not suitable for the practical application. Accordingly, more effort is encouraged to develop systematic methodologies for determining the corrosion kinetics of nZVI under practical circumstance.

(ii) The long-term fate and decontamination performance is closely related to the corrosion behavior of nZVI in water. Previous studies mainly focus on the investigation of iron corrosion in water or the pollutant removal capacity independently, but ignore the elucidation of iron corrosion during the contaminant removal process.

Hence, future studies on the establishment of relationship model between decontamination kinetics and corrosion kinetics is essential to determine the dosing time and dosage of nZVI reagent in practical application.

(iii) A major issue when considering the potential of nZVI for practical application is the electron utilization efficiency. In most application scenarios, extravagant iron corrosion leads to the unwanted electron waste. Hence, it is necessary to make more efforts on the modification strategies to prevent the side reaction between nZVI and water.

(iv) In-depth research on the migration and eco-toxicity of (modified-) nZVI corrosion products carrying contaminants is also required for guiding the rational design of robust nZVI with precisely tailored properties.

Declaration of Competing Interest

The authors declare that they have no known competing financial interests or personal relationships that could have appeared to influence the work reported in this paper.

Acknowledgments

This work was supported by the National Natural Science Foundation of China (No. 52200184) and the Fundamental Research Funds for Central Universities (No. 12060096014).

REFERENCES

Al-Hinai, A.T., Al-Hinai, M.H., Dutta, J., 2014. Application of Eh-pH diagram for room temperature precipitation of zinc stannate microcubes in an aqueous media. Mater. Res. Bull. 49, 645–650.

Bae, S., Collins, R.N., Waite, T.D., Hanna, K., 2018. Advances in surface passivation of nanoscale zerovalent iron: a critical review. Environ. Sci. Technol. 52 (21), 12010–12025.

Bae, S., Hanna, K., 2015. Reactivity of nanoscale zero-valent iron in unbuffered systems: effect of pH and Fe(II) dissolution. Environ. Sci. Technol. 49 (17), 10536–10543.

Chekli, L., Bayatsarmadi, B., Sekine, R., Sarkar, B., Shen, A.M., Scheckel, K.G., et al., 2016. Analytical characterisation of nanoscale zero-valent iron: a methodological review. Anal. Chim. Acta 903, 13–35.

Dong, H., Guan, X., Lo, I.M.C., 2012. Fate of As(V)-treated nano zero-valent iron: determination of arsenic desorption potential under varying environmental conditions by phosphate extraction. Water Res. 46 (13), 4071–4080.

Dong, H., Jiang, Z., Deng, J., Zhang, C., Cheng, Y., Hou, K., et al., 2018a. Physicochemical transformation of Fe/Ni bimetallic nanoparticles during aging in simulated groundwater and the consequent effect on contaminant removal. Water Res. 129, 51–57.

Dong, H., Li, L., Wang, Y., Ning, Q., Wang, B., Zeng, G., 2020. Aging of zero-valent iron-based nanoparticles in aqueous environment and the consequent effects on their reactivity and toxicity. Water Environ. Res. 92 (5), 646–661.

Dong, H., Zhang, C., Deng, J., Jiang, Z., Zhang, L., Cheng, Y., et al., 2018b. Factors influencing degradation of trichloroethylene by sulfide-modified nanoscale zero-valent iron in aqueous solution. Water Res. 135, 1–10.

Dong, H., Zhao, F., He, Q., Xie, Y., Zeng, Y., Zhang, L., et al., 2017. Physicochemical transformation of carboxymethyl cellulose-coated zero-valent iron nanoparticles (nZVI) in simulated groundwater under anaerobic conditions. Sep. Purif. Technol. 175, 376–383.

Dong, H., Zhao, F., Zeng, G., Tang, L., Fan, C., Zhang, L., et al., 2016. Aging study on carboxymethyl cellulose-coated zero-valent iron nanoparticles in water: chemical transformation and structural evolution. J. Hazard. Mater. 312, 234–242.

Du, J., Bao, J., Lu, C., Werner, D., 2016. Reductive sequestration of chromate by hierarchical FeS@Fe^0 particles. Water Res. 102, 73–81.

Fan, D., Anitori, R.P., Tebo, B.M., Tratnyek, P.G., Lezama Pacheco, J.S., Kukkadapu, R.K., et al., 2013. Reductive sequestration of pertechnetate ($^{99}TcO_4^-$) by nano zerovalent iron (nZVI) transformed by abiotic sulfide. Environ. Sci. Technol. 47 (10), 5302–5310.

Fan, D., Chen, S., Johnson, R.L., Tratnyek, P.G., 2015. Field deployable chemical redox probe for quantitative characterization of carboxymethylcellulose modified nano zerovalent iron. Environ. Sci. Technol. 49 (17), 10589–10597.

Fan, D., Lan, Y., Tratnyek, P.G., Johnson, R.L., Filip, J., O'Carroll, D.M., et al., 2017. Sulfidation of iron-based materials: a review of processes and implications for water treatment and remediation. Environ. Sci. Technol. 51 (22), 13070–13085.

Fan, D., O'Brien Johnson, G., Tratnyek, P.G., Johnson, R.L., 2016. Sulfidation of nano zerovalent iron (nZVI) for improved selectivity during in-situ chemical reduction (ISCR). Environ. Sci. Technol. 50 (17), 9558–9565.

Filip, J., Karlický, F., Marušák, Z., Lazar, P., Černík, M., Otyepka, M., et al., 2014. Anaerobic reaction of nanoscale zerovalent iron with water: mechanism and kinetics. J. Phys. Chem. C 118 (25), 13817–13825.

Gankanda, A., Rentz, N.S., Greenlee, L.F., 2019. Influence of ligand size and chelation strength on zerovalent iron nanoparticle adsorption and oxidation behavior in the presence of water vapor and liquid water. J. Phys. Chem. C 123 (4), 2474–2487.

Garcia, A.N., Zhang, Y., Ghoshal, S., He, F., O'Carroll, D.M., 2021. Recent advances in sulfidated zerovalent iron for contaminant transformation. Environ. Sci. Technol. 55 (13), 8464–8483.

Gomes, H.I., Dias-Ferreira, C., Ribeiro, A.B., Pamukcu, S., 2014. Influence of electrolyte and voltage on the direct current enhanced transport of iron nanoparticles in clay. Chemosphere 99, 171–179.

Greenlee, L.F., Torrey, J.D., Amaro, R.L., Shaw, J.M., 2012. Kinetics of zero valent iron nanoparticle oxidation in oxygenated water. Environ. Sci. Technol. 46 (23), 12913–12920.

Grieger, K.D., Fjordbøge, A., Hartmann, N.B., Eriksson, E., Bjerg, P.L., Baun, A., 2010. Environmental benefits and risks of zero-valent iron nanoparticles (nZVI) for in situ remediation: risk mitigation or trade-off? J. Contam. Hydrol. 118 (3-4), 165–183.

He, D., Ma, J., Collins, R.N., Waite, T.D., 2016a. Effect of structural transformation of nanoparticulate zero-valent iron on generation of reactive oxygen species. Environ. Sci. Technol. 50 (7), 3820–3828.

He, D., Ma, X., Jones, A.M., Ho, L., Waite, T.D., 2016b. Mechanistic and kinetic insights into the ligand-promoted depassivation of bimetallic zero-valent iron nanoparticles. Environ. Sci.: Nano 3 (4), 737–744.

Hu, Y., Zhang, M., Qiu, R., Li, X., 2018. Encapsulating nanoscale zero-valent iron with a soluble $Mg(OH)_2$ shell for improved mobility and controlled reactivity release. J. Mater. Chem. A 6 (6), 2517–2526.

Hua, Y., Liu, J., Gu, T., Wang, W., Zhang, W., 2018a. The colorful chemistry of nanoscale zero-valent iron (nZVI). J. Environ. Sci. 67, 1–3.

Hua, Y., Wang, W., Huang, X., Gu, T., Ding, D., Ling, L., et al., 2018b. Effect of bicarbonate on aging and reactivity of nanoscale zerovalent iron (nZVI) toward uranium removal. Chemosphere 201, 603–611.

Huang, H.H., 2016. The Eh-pH diagram and its advances. Metals 6 (1), 23.
Huang, P., Ye, Z., Xie, W., Chen, Q., Li, J., Xu, Z., Yao, M., 2013. Rapid magnetic removal of aqueous heavy metals and their relevant mechanisms using nanoscale zero valent iron (nZVI) particles. Water Res. 47 (12), 4050–4058.
Huang, X., Ling, L., Zhang, W., 2018. Nanoencapsulation of hexavalent chromium with nanoscale zero-valent iron: high resolution chemical mapping of the passivation layer. J. Environ. Sci. 67, 4–13.
Hug, S.J., Leupin, O., 2003. Iron-catalyzed oxidation of arsenic(III) by oxygen and by hydrogen peroxide: pH-dependent formation of oxidants in the fenton reaction. Environ. Sci. Technol. 37 (12), 2734–2742.
Johnson, R.L., Nurmi, J.T., O'Brien Johnson, G.S., Fan, D., O'Brien Johnson, R.L., Shi, Z., Salter-Blanc, A.J., Tratnyek, P.G., Lowry, G.V., 2013. Field-scale transport and transformation of carboxymethylcellulose-stabilized nano zero-valent iron. Environ. Sci. Technol. 47 (3), 1573–1580.
Jones, B., 2001. Evaluation of immobilized redox indicators as reversible, in situ redox sensors for determining Fe(III)-reducing conditions in environmental samples. Talanta 55 (4), 699–714.
Kallel, M., Belaid, C., Mechichi, T., Ksibi, M., Elleuch, B., 2009. Removal of organic load and pHenolic compounds from olive mill wastewater by Fenton oxidation with zero-valent iron. Chem. Eng. J. 150 (2-3), 391–395.
Kanel, S.R., Manning, B., Charlet, L., Choi, H., 2005. Removal of arsenic(III) from groundwater by nanoscale zero-valent iron. Environ. Sci. Technol. 39 (5), 1291–1298.
Kim, C., Chin, Y.-P., Ahn, J.-Y., Wei-Haas, M., McAdams, B., Hwang, I., 2018. Reciprocal influences of dissolved organic matter and nanosized zero-valent iron in aqueous media. Chemosphere 193, 936–942.
Kim, H., Hong, H.-J., Jung, J., Kim, S.-H., Yang, J.-W., 2010. Degradation of trichloroethylene (TCE) by nanoscale zero-valent iron (nZVI) immobilized in alginate bead. J. Hazard. Mater. 176 (1-3), 1038–1043.
Kim, H.-S., Ahn, J.-Y., Kim, C., Lee, S., Hwang, I., 2014. Effect of anions and humic acid on the performance of nanoscale zero-valent iron particles coated with polyacrylic acid. Chemosphere 113, 93–100.
Kim, H.-S., Kim, T., Ahn, J.-Y., Hwang, K.-Y., Park, J.-Y., Lim, T.-T., Hwang, I., 2012. Aging characteristics and reactivity of two types of nanoscale zero-valent iron particles (Fe^{BH} and Fe^{H2}) in nitrate reduction. Chem. Eng. J. 197, 16–23.
Klimkova, S., Cernik, M., Lacinova, L., Filip, J., Jancik, D., Zboril, R., 2011. Zero-valent iron nanoparticles in treatment of acid mine water from in situ uranium leaching. Chemosphere 82 (8), 1178–1184.
Lei, C., Sun, Y., Tsang, D.C.W., Lin, D., 2018. Environmental transformations and ecological effects of iron-based nanoparticles. Environ. Pollut. 232, 10–30.
Li, B., He, Z., Zhou, H., Zhang, H., Cheng, T., 2017a. Reversible fluorescent probes for chemical and biological redox process. Chin. Chem. Lett. 28 (10), 1929–1934.
Li, J., Guan, X., Zhang, W., 2021a. Architectural genesis of metal(loid)s with iron nanoparticle in water. Environ. Sci. Technol. 55, 12801–12808.
Li, J., Zhang, X., Sun, Y., Liang, L., Pan, B., Zhang, W., Guan, X., 2017b. Advances in sulfidation of zerovalent iron for water decontamination. Environ. Sci. Technol. 51 (23), 13533–13544.
Li, J, Zhou, Q., Wu, Y., Yuan, Y., Liu, Y., 2018. Investigation of nanoscale zerovalent iron-based magnetic and thermal dual-responsive composite materials for the removal and detection of phenols. Chemosphere 195, 472–482.
Li, L., Li, Y., Xu, C., Papangelakis, V.G., Chu, G., Li, G., Wang, X., Kong, L., 2014. Eh–pH diagrams from 333.15 to 453.15 K for lithium–titanium composite oxides and their synthesis in aqueous solution. Hydrometallurgy 142, 131–136.
Li, M., Shang, H., Li, H., Hong, Y., Ling, C., Wei, K., Zhou, B., Mao, C., Ai, Z., Zhang, L., 2021b. Kirkendall effect boosts phosphorylated nZVI for efficient heavy metal wastewater treatment. Angew. Chem. Int. Ed. 60 (31), 17115–17122.
Li, S., Wang, W., Liang, F., Zhang, W., 2017c. Heavy metal removal using nanoscale zero-valent iron (nZVI): Theory and application. J. Hazard. Mater. 322, 163–171.
Li, X., Zhang, W., 2006. Iron nanoparticles: The core-shell structure and unique properties for Ni(II) sequestration. Langmuir 22 (10), 4638–4642.
Li, X., Zhang, M., Liu, Y., Li, X., Liu, Y., Hua, R., He, C., 2013. Removal of U(VI) in aqueous solution by nanoscale zero-valent iron(nZVI). Water Qual. Expos. Health 5 (1), 31–40.
Ling, L., Huang, X., Li, M., Zhang, W., 2017. Mapping the reactions in a single zero-valent iron nanoparticle. Environ. Sci. Technol. 51 (24), 14293–14300.
Ling, L., Huang, X.-Y., Zhang, W.-X., 2018a. Enrichment of precious metals from wastewater with core-shell nanoparticles of iron. Adv. Mater. 30 (17), 1705703.
Ling, L., Pan, B., Zhang, W., 2015. Removal of selenium from water with nanoscale zero-valent iron: Mechanisms of intraparticle reduction of Se(IV). Water Res. 71, 274–281.
Ling, L., Tang, C., Zhang, W., 2018b. Visualization of silver nanoparticle formation on nanoscale zero-valent iron. Environ. Sci. Technol. Lett. 5 (8), 520–525.
Ling, L., Zhang, W., 2017. Visualizing arsenate reactions and encapsulation in a single zero-valent iron nanoparticle. Environ. Sci. Technol. 51 (4), 2288–2294.
Ling, L., Zhang, W., 2015. Enrichment and encapsulation of uranium with iron nanoparticle. J. Am. Chem. Soc. 137 (8), 2788–2791.
Ling, L., Zhang, W., 2014a. Sequestration of arsenate in zero-valent iron nanoparticles: visualization of intraparticle reactions at angstrom resolution. Environ. Sci. Technol. Lett. 1 (7), 305–309.
Ling, L., Zhang, W., 2014b. Reactions of nanoscale zero-valent iron with Ni(II): three-dimensional tomography of the "hollow out" effect in a single nanoparticle. Environ. Sci. Technol. Lett. 1 (3), 209–213.
Liu, A., Liu, J., Han, J., Zhang, W., 2017. Evolution of nanoscale zero-valent iron (nZVI) in water: microscopic and spectroscopic evidence on the formation of nano- and micro-structured iron oxides. J. Hazard. Mater. 322, 129–135.
Liu, A., Liu, J., Pan, B., Zhang, W., 2014. Formation of lepidocrocite (γ-FeOOH) from oxidation of nanoscale zero-valent iron (nZVI) in oxygenated water. RSC Adv. 4 (101), 57377–57382.
Liu, A., Liu, J., Zhang, W., 2015. Transformation and composition evolution of nanoscale zero valent iron (nZVI) synthesized by borohydride reduction in static water. Chemosphere 119, 1068–1074.
Liu, A., Wang, W., Liu, J., Fu, R., Zhang, W., 2018. Nanoencapsulation of arsenate with nanoscale zero-valent iron (nZVI): a 3D perspective. Sci. Bull. 63 (24), 1641–1648.
Liu, A.-R., Wakayama, T., Nakamura, C., Miyake, J., Zorin, N.A., Qian, D.-J., 2007. Electrochemical properties of carbon nanotubes–hydrogenase conjugates Langmuir–Blodgett films. Electrochim. Acta 52 (9), 3222–3228.
Liu, H.B., Chen, T.H., Chang, D.Y., Chen, D., Liu, Y., He, H.P., Yuan, P., Frost, R., 2012. Nitrate reduction over nanoscale zero-valent iron prepared by hydrogen reduction of goethite. Mater. Chem. Phys. 133 (1), 205–211.
Liu, J., Liu, A., Zhang, W., 2016. The influence of polyelectrolyte modification on nanoscale zero-valent iron (nZVI): aggregation, sedimentation, and reactivity with Ni(II) in water. Chem. Eng. J. 303, 268–274.
Liu, Y., Lowry, G.V., 2006. Effect of particle age (Fe° Content) and solution pH on NZVI reactivity: H_2 evolution and TCE dechlorination. Environ. Sci. Technol. 40 (19), 6085–6090.

Liu, Y., Majetich, S.A., Tilton, R.D., Sholl, D.S., Lowry, G.V., 2005. TCE dechlorination rates, pathways, and efficiency of nanoscale iron particles with different properties. Environ. Sci. Technol. 39 (5), 1338–1345.

Lv, D., Zhou, X., Zhou, J., Liu, Y., Li, Y., Yang, K., Lou, Z., Baig, S.A., Wu, D., Xu, X., 2018. Design and characterization of sulfide-modified nanoscale zerovalent iron for cadmium(II) removal from aqueous solutions. Appl. Surf. Sci. 442, 114–123.

Lv, X., Hu, Y., Tang, J., Sheng, T., Jiang, G., Xu, X., 2013. Effects of co-existing ions and natural organic matter on removal of chromium (VI) from aqueous solution by nanoscale zero valent iron (nZVI)-Fe_3O_4 nanocomposites. Chem. Eng. J. 218, 55–64.

Ma, L., Yan, J., Gan, M., Qiu, W., He, L., Li, J., 2008. Application of QCM technique in the kinetic study of polyaniline film formation in the presence of a constant (0.4 T) magnetic field. Polym. Test. 27 (6), 683–687.

Mangayayam, M.C., Perez, J.P.H., Dideriksen, K., Freeman, H.M., Bovet, N., Benning, L.G., Tobler, D.J., 2019. Structural transformation of sulfidized zerovalent iron and its impact on long-term reactivity. Environ. Sci.: Nano 6 (11), 3422–3430.

Monhemius, A.J., 2017. The iron elephant: A brief history of hydrometallurgists' struggles with element no. 26. CIM. J. 8, 197–206.

Moon, B.-H., Park, Y.-B., Park, K.-H., 2011. Fenton oxidation of Orange II by pre-reduction using nanoscale zero-valent iron. Desalination 268 (1-3), 249–252.

Mueller, N.C., Braun, J., Bruns, J., Černík, M., Rissing, P., Rickerby, D., Nowack, B., 2012. Application of nanoscale zero valent iron (NZVI) for groundwater remediation in Europe. Environ. Sci. Pollut. Res. 19 (2), 550–558.

Nurmi, J.T., Tratnyek, P.G., 2008. Electrochemical studies of packed iron powder electrodes: effects of common constituents of natural waters on corrosion potential. Corros. Sci. 50 (1), 144–154.

O'Carroll, D., Sleep, B., Krol, M., Boparai, H., Kocur, C., 2013. Nanoscale zero valent iron and bimetallic particles for contaminated site remediation. Adv. Water Resour. 51, 104–122.

Okur, S., Kuş, M., Özel, F., Aybek, V., Yılmaz, M., 2010. Humidity adsorption kinetics of calix[4]arene derivatives measured using QCM technique. Talanta 81 (1-2), 248–251.

Ortega-Borges, R., Lincot, D., 1993. Mechanism of chemical bath deposition of cadmium sulfide thin films in the ammonia-thiourea system: in situ kinetic study and modelization. J. Electrochem. Soc. 140 (12), 3464–3473.

Phenrat, T., Saleh, N., Sirk, K., Tilton, R.D., Lowry, G.V., 2007. Aggregation and sedimentation of aqueous nanoscale zerovalent iron dispersions. Environ. Sci. Technol. 41 (1), 284–290.

Pullin, H., Crane, R.A., Morgan, D.J., Scott, T.B., 2017a. The effect of common groundwater anions on the aqueous corrosion of zero-valent iron nanoparticles and associated removal of aqueous copper and zinc. J. Environ. Chem. Eng. 5 (1), 1166–1173.

Pullin, H., Springell, R., Parry, S., Scott, T., 2017b. The effect of aqueous corrosion on the structure and reactivity of zero-valent iron nanoparticles. Chem. Eng. J. 308, 568–577.

Qi, Y., Li, X., He, Y., Zhang, D., Ding, J., 2019. Mechanism of acceleration of iron corrosion by a polylactide coating. ACS Appl. Mater. Int. 11 (1), 202–218.

Qin, H., Guan, X., Bandstra, J.Z., Johnson, R.L., Tratnyek, P.G., 2018. Modeling the kinetics of hydrogen formation by zerovalent iron: effects of sulfidation on micro- and nano-scale particles. Environ. Sci. Technol. 52 (23), 13887–13896.

Qiu, W., Huang, H., Zeng, S., Xue, T., Liu, J., 2011. A kinetic study of in situ polyaniline–gold composite film formation. J. Polym. Res. 18 (1), 19–23.

Rajajayavel, S.R.C., Ghoshal, S., 2015. Enhanced reductive dechlorination of trichloroethylene by sulfidated nanoscale zerovalent iron. Water Res. 78, 144–153.

Reardon, E.J., 2014. Capture and storage of hydrogen gas by zero-valent iron. J. Contam. Hydrol. 157, 117–124.

Reardon, E.J., Fagan, R., Vogan, J.L., Przepiora, A., 2008. Anaerobic corrosion reaction kinetics of nanosized iron. Environ. Sci. Technol. 42 (7), 2420–2425.

Reinsch, B.C., Forsberg, B., Penn, R.L., Kim, C.S., Lowry, G.V., 2010. Chemical transformations during aging of zerovalent iron nanoparticles in the presence of common groundwater dissolved constituents. Environ. Sci. Technol. 44 (9), 3455–3461.

Ryu, A., Jeong, S.-W., Jang, A., Choi, H., 2011. Reduction of highly concentrated nitrate using nanoscale zero-valent iron: effects of aggregation and catalyst on reactivity. Appl. Catal. B Environ. 105 (1-2), 128–135.

Sarathy, V., Tratnyek, P.G., Nurmi, J.T., Baer, D.R., Amonette, J.E., Chun, C.L., Penn, R.L., Reardon, E.J., 2008. Aging of iron nanoparticles in aqueous solution: effects on structure and reactivity. J. Phys. Chem. C 112 (7), 2286–2293.

Sauerbrey, G., 1959. Verwendung von schwingquarzen zur wägung dünner schichten und zur mikrowägung. Z. Phys. 155 (2), 206–222.

Shi, Z., Fan, D., Johnson, R.L., Tratnyek, P.G., Nurmi, J.T., Wu, Y., Williams, K.H., 2015. Methods for characterizing the fate and effects of nano zerovalent iron during groundwater remediation. J. Contam. Hydrol. 181, 17–35.

Shi, Z., Nurmi, J.T., Tratnyek, P.G., 2011. Effects of nano zero-valent iron on oxidation-reduction potential. Environ. Sci. Technol. 45 (4), 1586–1592.

Shu, H.-Y., Chang, M.-C., Yu, H.-H., Chen, W.-H., 2007. Reduction of an azo dye Acid Black 24 solution using synthesized nanoscale zerovalent iron particles. J. Colloid. Interf. Sci. 314 (1), 89–97.

Sohn, K., Kang, S.W., Ahn, S., Woo, M., Yang, S.-K., 2006. Fe(0) Nanoparticles for nitrate reduction: stability, reactivity, and transformation. Environ. Sci. Technol. 40 (17), 5514–5519.

Su, Y., Adeleye, A.S., Huang, Y., Sun, X., Dai, C., Zhou, X., Zhang, Y., Keller, A.A., 2014. Simultaneous removal of cadmium and nitrate in aqueous media by nanoscale zerovalent iron (nZVI) and Au doped nZVI particles. Water Res. 63, 102–111.

Su, Y., Jassby, D., Song, S., Zhou, X., Zhao, H., Filip, J., Petala, E., Zhang, Y., 2018. Enhanced oxidative and adsorptive removal of diclofenac in heterogeneous Fenton-like reaction with sulfide modified nanoscale zerovalent iron. Environ. Sci. Technol. 52 (11), 6466–6475.

Tang, C., Ling, L., Zhang, W., 2021. Visualizing trace pollutants in solids at nanoscale via electron tomography. Environ. Sci. Technol. 55 (17), 11533–11537.

Tang, C., Ling, L., Zhang, W., 2020. Pb(II) deposition-reduction-growth onto iron nanoparticles induced by graphitic carbon nitride. Chem. Eng. J. 387, 124088.

Torrey, J.D., Killgore, J.P., Bedford, N.M., Greenlee, L.F., 2015a. Oxidation behavior of zero-valent iron nanoparticles in mixed matrix water purification membranes. Environ. Sci.: Water Res. Technol. 1 (2), 146–152.

Torrey, J.D., Kirschling, T.L., Greenlee, L.F., 2015b. Processing and characterization of nanoparticle coatings for quartz crystal microbalance measurements. J. Res. Natl. Inst. Stan. 120, 1.

Tratnyek, P.G., Reilkoff, T.E., Lemon, A.W., Scherer, M.M., Balko, B.A., Feik, L.M., Henegar, B.D., 2001. Visualizing redox chemistry: probing environmental oxidation–reduction reactions with indicator dyes. Chem. Educ. 6 (3), 172–179.

Tratnyek, P.G., Salter-Blanc, A.J., Nurmi, J.T., Amonette, J.E., Liu, J., Wang, C., Dohnalkova, A., Baer, D.R., 2011. Reactivity of zerovalent metals in aquatic media: effects of organic surface coatings. In: ACS Symposium Series. American Chemical Society, Washington, DC, pp. 381–406.

Turcio-Ortega, D., Fan, D., Tratnyek, P.G., Kim, E.-J., Chang, Y.-S., 2012. Reactivity of Fe/FeS nanoparticles: electrolyte composition effects on corrosion electrochemistry. Environ. Sci. Technol. 46 (22), 12484–12492.

Velimirovic, M., Carniato, L., Simons, Q., Schoups, G., Seuntjens, P., Bastiaens, L., 2014. Corrosion rate estimations of microscale zerovalent iron particles via direct hydrogen production measurements. J. Hazard. Mater. 270, 18–26.

Wang, J., Liu, G., Li, T., Zhou, C., Qi, C., 2015. Zero-valent iron nanoparticles (NZVI) supported by kaolinite for Cu^{II} and Ni^{II} ion removal by adsorption: kinetics, thermodynamics, and mechanism. Aust. J. Chem. 68, 1305.

Wang, S., Gao, B., Li, Y., Creamer, A.E., He, F., 2017. Adsorptive removal of arsenate from aqueous solutions by biochar supported zero-valent iron nanocomposite: batch and continuous flow tests. J. Hazard. Mater. 322, 172–181.

Wang, W., Hua, Y., Li, S., Yan, W., Zhang, W., 2016. Removal of Pb(II) and Zn(II) using lime and nanoscale zero-valent iron (nZVI): a comparative study. Chem. Eng. J. 304, 79–88.

Wen, Z., Zhang, Y., Dai, C., 2014. Removal of phosphate from aqueous solution using nanoscale zerovalent iron (nZVI). Colloids Surf. A Physicochem. Eng. Asp. 457, 433–440.

Wu, C., Liu, W., Zhang, J., Chu, S., Shi, Z., Dang, Z., Lin, Z., 2017a. Mechanisms of synergistic removal of low concentration As(V) by nZVI@$Mg(OH)_2$ nanocomposite. J. Phys. Chem. C 121 (39), 21411–21419.

Wu, C., Tu, J., Liu, W., Zhang, J., Chu, S., Lu, G., Lin, Z., Dang, Z., 2017b. The double influence mechanism of pH on arsenic removal by nano zero valent iron: electrostatic interactions and the corrosion of Fe^0. Environ. Sci.: Nano 4 (7), 1544–1552.

Wu, D., Shen, Y., Ding, A., Qiu, M., Yang, Q., Zheng, S., 2013. Phosphate removal from aqueous solutions by nanoscale zero-valent iron. Environ. Technol. 34 (18), 2663–2669.

Wu, M., Ma, Y., Wan, J., Wang, Y., Guan, Z., Yan, Z., 2019. Investigation of factors affecting the physicochemical properties and degradation performance of nZVI@mesoSiO$_2$ nanocomposites. J. Mater. Sci. 54 (10), 7483–7502.

Xia, X., Ling, L., Zhang, W., 2017. Solution and surface chemistry of the Se(IV)-Fe(0) reactions: effect of initial solution pH. Chemosphere 168, 1597–1603.

Xiao, S., Jin, Z., Dong, H., Xiao, J., Li, Y., Li, L., Li, R., Chen, J., Tian, R., Xie, Q., 2022. A comparative study on the physicochemical properties, reactivity and long-term performance of sulfidized nanoscale zerovalent iron synthesized with different kinds of sulfur precursors and procedures in simulated groundwater. Water Res. 212, 118097.

Xie, Y., Fang, Z., Qiu, X., Tsang, E.P., Liang, B., 2014. Comparisons of the reactivity, reusability and stability of four different zero-valent iron-based nanoparticles. Chemosphere 108, 433–436.

Xin, J., Tang, F., Zheng, X., Shao, H., Kolditz, O., Lu, X., 2016. Distinct kinetics and mechanisms of mZVI particles aging in saline and fresh groundwater: H_2 evolution and surface passivation. Water Res. 100, 80–87.

Xu, J., Avellan, A., Li, H., Clark, E.A., Henkelman, G., Kaegi, R., Lowry, G.V., 2020a. Iron and sulfur precursors affect crystalline structure, speciation, and reactivity of sulfidized nanoscale zerovalent iron. Environ. Sci. Technol. 54 (20), 13294–13303.

Xu, J., Avellan, A., Li, H., Liu, X., Noël, V., Lou, Z., Wang, Y., Kaegi, R., Henkelman, G., Lowry, G.V., 2020b. Sulfur loading and speciation control the hydrophobicity, electron transfer, reactivity, and selectivity of sulfidized nanoscale zerovalent iron. Adv. Mater. 32 (17), 1906910.

Xu, J., Cao, Z., Zhou, H., Lou, Z., Wang, Y., Xu, X., Lowry, G.V., 2019a. Sulfur dose and sulfidation time affect reactivity and selectivity of post-sulfidized nanoscale zerovalent iron. Environ. Sci. Technol. 53 (22), 13344–13352.

Xu, J., Li, H., Lowry, G.V., 2021. Sulfidized nanoscale zero-valent iron: tuning the properties of this complex material for efficient groundwater remediation. Acc. Mater. Res. 2 (6), 420–431.

Xu, J., Wang, Y., Weng, C., Bai, W., Jiao, Y., Kaegi, R., Lowry, G.V., 2019b. Reactivity, selectivity, and long-term performance of sulfidized nanoscale zerovalent iron with different properties. Environ. Sci. Technol. 53 (10), 5936–5945.

Yan, W., Herzing, A.A., Kiely, C.J., Zhang, W., 2010a. Nanoscale zero-valent iron (nZVI): aspects of the core-shell structure and reactions with inorganic species in water. J. Contam. Hydrol. 118 (3-4), 96–104.

Yan, W., Herzing, A.A., Li, X., Kiely, C.J., Zhang, W., 2010b. Structural evolution of Pd-doped nanoscale zero-valent iron (nZVI) in aqueous media and implications for particle aging and reactivity. Environ. Sci. Technol. 44 (11), 4288–4294.

Yang, X., Zhang, C., Liu, F., Tang, J., 2021. Groundwater geochemical constituents controlling the reductive dechlorination of TCE by nZVI: evidence from diverse anaerobic corrosion mechanisms of nZVI. Chemosphere 262, 127707.

Yang, X., Zhang, C., Liu, F., Tang, J., Huang, F., Zhang, L., 2019. Diversity in the species and fate of chlorine during TCE reduction by two nZVI with non-identical anaerobic corrosion mechanism. Chemosphere 230, 230–238.

Zhang, J., Cheng, Z., Yang, X., Luo, J., Li, H., Chen, H., Zhang, Q., Li, J., 2020. Mediating the reactivity and selectivity of nanoscale zerovalent iron toward nitrobenzene under porous carbon confinement. Chem. Eng. J. 393, 124779.

Zhang, S.-H., Wu, M.-F., Tang, T.-T., Xing, Q.-J., Peng, C.-Q., Li, F., Liu, H., Luo, X.-B., Zou, J.-P., Min, X.-B., Luo, J.-M., 2018a. Mechanism investigation of anoxic Cr(VI) removal by nano zero-valent iron based on XPS analysis in time scale. Chem. Eng. J. 335, 945–953.

Zhang, Y., Zhi, Y., Liu, J., Ghoshal, S., 2018b. Sorption of perfluoroalkyl acids to fresh and aged nanoscale zerovalent iron particles. Environ. Sci. Technol. 52 (11), 6300–6308.